Astronomy & Astrophysics manuscript no. he
August 3, 2016
©ESO 2016

arXiv:1608.00838v1 [astro-ph.SR] 2 Aug 2016

The cause of spatial structure in solar He I 1083 nm multiplet images

Jorrit Leenaarts[1], Thomas Golding[2], Mats Carlsson[2], Tine Libbrecht[1], and Jayant Joshi[1]

[1] Institute for Solar Physics, Department of Astronomy, Stockholm University, AlbaNova University Centre, SE-106 91 Stockholm Sweden, e-mail: jorrit.leenaarts@astro.su.se,tine.libbrecht@astro.su.se,jayant.joshi@astro.su.se,
[2] Institute of Theoretical Astrophysics, University of Oslo, P.O. Box 1029 Blindern, N–0315 Oslo, Norway e-mail: mats.carlsson@astro.uio.no,thomas.golding@astro.uio.no

Received ; accepted

ABSTRACT

Context. The He I 1083 nm is a powerful diagnostic for inferring properties of the upper solar chromosphere, in particular for the magnetic field. The basic formation of the line in one-dimensional models is well understood, but the influence of the complex three-dimensional structure of the chromosphere and corona has however never been investigated. This structure must play an essential role because images taken in He I 1083 nm show structures with widths down to 100 km.
Aims. To understand the effect of the three-dimensional temperature and density structure in the solar atmosphere on the formation of the He I 1083 nm line.
Methods. We solve the non-LTE radiative transfer problem assuming statistical equilibrium for a simple 9-level helium atom that nevertheless captures all essential physics. As a model atmosphere we use a snapshot from a 3D radiation-MHD simulation computed with the *Bifrost* code. Ionising radiation from the corona is self-consistently taken into account.
Results. The emergent intensity in the He I 1083 nm is set by the source function and the opacity in the upper chromosphere. The former is dominated by scattering of photospheric radiation and does not vary much with spatial location. The latter is determined by the photonionisation rate in the He I ground state continuum, as well as the electron density in the chromosphere. The spatial variation of the flux of ionising radiation is caused by the spatially-structured emissivity of the ionising photons from material at $T \approx 100$ kK in the transition region. The hotter coronal material produces more ionising photons, but the resulting radiation field is smooth and does not lead to small-scale variation of the UV flux. The corrugation of the transition region further increases the spatial variation of the amount of UV radiation in the chromosphere. Finally we find that variations in the chromospheric electron density also cause strong variation in He I 1083 nm opacity. We compare our findings to observations using SST, IRIS and SDO/AIA data.

Key words. Sun: atmosphere – Sun: chromosphere – Radiative transfer

1. Introduction

The He I 1083 nm multiplet arises from the three radiative transitions between the $1s2s\,^3S$ and $1s2p\,^3P$ triplet terms of neutral helium. In the solar spectrum it appears as two absorption lines at 1082.91 nm and 1083.03 nm (in air). Because of the large energy difference between the lower level of the multiplet and the singlet ground state (19.8 eV), the population of the lower level cannot be caused by electron collisions at typical chromospheric temperatures of $\sim$ 10 kK. This led Goldberg (1939) to propose that photoionisation from the He I ground state continuum ($\lambda < 50.4$ nm) follow by spontaneous recombination (often called PR mechanism) is the driver of triplet population. Observational evidence from solar observations is the general correlation of X-ray emission and He I 1083 nm absorption (Kahler et al. 1983). Observations of weakly active dwarfs, giants and supergiant stars of spectral type F7 or later show a correlation between X-ray flux and He I 1083 nm equivalent width (Zarro & Zirin 1986). The same relation has been established for active giants, but interestingly, not for active dwarfs (Sanz-Forcada & Dupree 2008).

The observational evidence has been supported by many calculations of increasing sophistication (e.g. Zirin 1975; Livshits et al. 1976; Pozhalova 1988; Avrett et al. 1994; Andretta & Jones 1997; Centeno et al. 2008), but all either in a plane-parallel slab geometry or using one-dimensional plane-parallel atmospheres without an actual corona. Consequently the coronal radiation field in these calculations had to be prescribed, for which typically the data described in Tobiska (1991) has been used. All models reproduced the observed correlation between the solar EUV flux and the He I 1083 nm equivalent width (EW, see Tobiska 1991). An interesting feature of the PR mechanism is that the 30.4 nm of He II line is the strongest line in the He I ground state continuum, so that the formation of the He I 1083 nm is influenced by the resonance lines of He II.

Livshits et al. (1976) demonstrated that the relative population density of the triplet system also depends on the electron density. By considering the dominant pathways that populate and depopulate the triplet system they found that the relative population of the triplet ground state $n(2s\,^3S)/n_{He}$ is approximately given by

$$\frac{n(2s\,^3S)}{n_{He}} = \frac{\alpha_t}{(1 + n_e\alpha_s/\phi_s)\,(\phi_t/n_e + q_{ts})}, \quad (1)$$

with α_t the photorecombination rate coefficient per electron into the triplet system, n_e the electron density, α_s the photorecomination rate coefficient per electron into the singlet system, ϕ_s and ϕ_t the photoionization rate coefficients for the $1s^2\,^1S$ and $1s2s\,^3S$ levels, and q_{ts} the electron collision rate coefficient per electron

from the 1s2s ^{3}S level into the 1s2p ^{1}P and 1s^2 ^{1}S singlet levels. The quantities α_t and α_s are approximately constant (exactly constant if stimulated recombination is ignored), ϕ_s depends on the radiation field blueward of 50.4 nm, α_t depends on the radiation field blueward of 259 nm, and q_{ts} depends on temperature.

The relative population is an increasing function of electron density for typical values of the upper chromospheric electron density (10^{15}–10^{18} m^{-3}) and temperature (10 kK) at fixed coronal UV illumination. We thus also expect variations in the He I 1083 nm strength caused by variations in the mass density and ionisation degree in the chromosphere.

An alternative mechanism for creating He I 1083 nm opacity is direct collisional excitation from the He I ground state to the lower level of the line. Owing to the large energy gap between the two levels this mechanism is inefficient in the chromosphere, but can act whenever the temperature is above 20,000 K, i.e, in the lower transition region. (e.g. Milkey et al. 1973). At those temperatures one expects little He I based on statistical equilibrium calculations, but it might be present due to slow ionization and recombination during rapidly changing thermodynamic properties and the a drift of He I atoms into areas with higher electron temperature in the presence of strong temperature gradients and a long mean time between collisions. Several authors have proposed such mechanisms to explain the intensities of the resonance lines of helium, such as He I 53.7 nm, He I 58.4 nm, He II 30.4 nm, and HeII 25.6 nm. (Milkey et al. 1973; Jordan 1975; Smith & Jordan 2002; Smith 2003; Pietarila & Judge 2004). Such effects also influence the formation of the He I 1083 nm in 1D radiation-hydrodynamics simulations (Golding et al. 2014).

The one-dimensional nature of the modelling efforts so far has meant that they are unable to explain the spatial structure of the He I 1083 nm equivalent width, besides the general conclusion that large EW corresponds to larger impinging EUV flux and/or larger chromospheric density.

High-resolution coronal images (e.g., Cirtain et al. 2013) show spatial structure down to 0.″2, indicating coronal temperature and/or density variations at least down to that scale, while the actual emitted spectrum below 50.4 nm strongly depends on temperature. This leads to a large variation in space of the emissivity of ionising radiation, and this should lead to a spatial variation of the ionising radiation impinging on the chromosphere. The transition region between the chromosphere and the corona is highly corrugated which will introduce additional differences in impinging flux as parts of the chromosphere can shield other parts from the coronal radiation.

Three-dimensional numerical simulations (e.g., Carlsson et al. 2016) as well as semi-empirical 1D models of the solar chromosphere (e.g., Fontenla et al. 2006) indicate that considerable density variations occur at the top of the chromosphere.

One thus expects strong spatial variation of the strength of the He I 1083 nm. This is indeed the case: high-resolution observations show spatial structure down to a fraction of an arcsecond (e.g. Ji et al. 2012; Schad et al. 2013, 2015).

In this paper we investigate the causes of the spatial variation of the He I 1083 nm strength with help of numerical simulations of the solar atmosphere, 3D non-LTE radiative transfer calculations, and observations taken with the Swedish 1-m Solar Telescope (SST) and the Interface Region Imaging Spectrograph (IRIS). Our aim is to investigate in detail the origin of the variation in ionising UV radiation as well as the influence of the corrugation of the transition region and the chromospheric electron density variation on He I 1083 nm images.

In Section 2 we describe our numerical simulation and the subsequent radiative transfer modelling. Section 3 describes our observations. We describe the relation between coronal UV radiation, chromospheric electron density and He I 1083 nm absorption in Section 4. Section 5 contains a brief observational test of our theoretical finding that He I 1083 nm absorption should correlate with Si IV emission, and we finish with a discussion in Section 6.

2. Numerical Method

Radiation-MHD simulation As a model atmosphere we use a snapshot from a three-dimensional radiation-MHD simulation computed with the *Bifrost* code (Gudiksen et al. 2011). This code solves the resistive-MHD equations together with heat conduction and non-LTE radiative losses on a Cartesian grid. The particular simulation that we use here is a 3D extension of the 2D simulations of Golding et al. (2016). It uses an equation-of-state (EOS) that takes the non-equilibrium ionisation of hydrogen and helium into account. Non-equilibrium ionisation has a strong effect on the temperature and density structure in the chromosphere and transition region, and is thus required to obtain a realistic model of the upper chromosphere (Carlsson & Stein 2002; Leenaarts et al. 2007; Golding et al. 2014, 2016).

The inclusion of the Lyman continuum and the Lyman alpha line in *Bifrost* is important because the hydrogen Lyman continuum is a source of ionising photons in the He I continuum. Treating these these transitions in detailed balance, as was done in earlier models (such as those described in Carlsson et al. 2016) leads to an erroneous amount of Lyman continuum photons in the subsequent radiative transfer step.

The simulation was run on a grid of $504 \times 504 \times 496$ points, with a horizontal domain size of 24×24 Mm^2. In the vertical direction the domain spans from 2.4 Mm below the average height of $< \tau_{500} >= 1$ to 12.4 Mm above it. Besides the different EOS the run has an identical setup to the publicly available simulation described in Carlsson et al. (2016). In short, the simulation was run using an LTE EOS for 1,750 s after an initial smooth bipolar magnetic field was introduced into a previously relaxed hydrodynamical simulation. This removed transients caused by the introduction of the magnetic field. Then the EOS was changed from LTE to non-equilibrium ionisation of hydrogen and helium, and the simulation was run for an additional 2,000 s. We took the snapshot 780 s after the non-equilibrium EOS was switched on. We refer the reader to Gudiksen et al. (2011), Golding et al. (2016), and Carlsson et al. (2016) for further details of the simulation.

Model atmosphere The *Bifrost* snapshot was reduced in size to a grid of $252 \times 252 \times 496$ by removing every second column in the two horizontal directions to reduce the computational cost of the radiative transfer computation.

Model atom We use the same helium model atom as Carlsson & Stein (2002). By collapsing the sublevels in each term to a collective level this atom has only nine states. In this way the atom includes the 1s^2, 1s2s, and 1s2p terms of the singlet system and the 1s2s and 1s2p terms of the triplet system of He I, the 1s, 2s and 2p terms of He II and a single state for He III. This model captures all pertinent processes despite its small size: it includes the bound-free transitions between the ground states that give rise to the ionisation edges at 22.8 nm and 50.4 nm, the He II 30.4 nm line, and a representative He I 1083 nm line. The latter

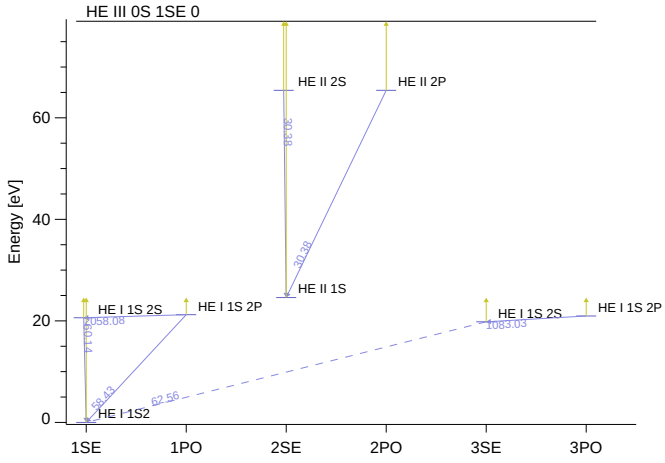

Fig. 1. Term diagram of our nine-level helium model atom. Solid blue lines indicate allowed radiative bound-bound transitions, dashed lines forbidden bound-bound transitions and yellowish lines radiative bound-free transitions.

does not have the three components (from the upper levels $2\,^3P_2$, $2\,^3P_1$, and $2\,^3P_0$ to the lower level $2\,^3S_1$) as in reality, but instead consist of a single transition at 1083.33 nm in vacuum with an oscillator strength $f = 0.539$. A term diagram of our model atom is shown in Fig. 1.

Radiative transfer The radiative transfer calculations are done with the *Multi3d* code (Leenaarts & Carlsson 2009). It solves the problem of non-LTE radiative transfer in full 3D using the formalism of Rybicki & Hummer (1991, 1992). The code is parallellized using MPI and employs domain decomposition in the three spatial dimensions as well as in frequency. The formal solution is computed on short characteristics using monotonic cubic Hermite polynomials (Auer 2003; Ibgui et al. 2013) to interpolate the source function and the extinction coefficient. Interpolation from grid points to cell interfaces is done using cubic convolution modified to avoid overshooting artefacts. As angle quadrature we use the A4 set from Carlson (1963), which contains 24 angles. We compute the background opacities, and background scattering probabilities in the photosphere and chromosphere for all elements except hydrogen and helium in LTE using the Uppsala opacity package (Gustafsson 1973). The hydrogen opacities and scattering probabilities are based on the non-equilibrium hydrogen populations from the *Bifrost* simulation (see Sec. 2) instead. Note that the background opacities include a scattering term assuming coherent scattering instead of complete redistribution. This assumption influences the Lyman-continuum intensities, which in turn has an effect on the photoionisation in the He I ground state continuum. Ideally one would like to run both hydrogen and helium simultaneously in full non-LTE, but this is currently not possible with *Multi3d*.

Applicability of statistical equilibrium for helium In Golding et al. (2014, 2016) we showed that the ionisation of helium is out of statistical equilibrium. Comparisons of one-dimensional calculations assuming SE and NE using the *RADYN* code (e.g., Carlsson & Stein 1992) indicate that significant differences in the He I 1083 nm profiles can occur between SE and NE calculations (see Fig. 9 of Golding et al. 2014). We therefore expect that the current SE calculations will be substantially different from a more physically correct NE calculation. The latter is however currently beyond our means. We focus here on the spatial structure of He I 1083 nm images caused by the spatial variation in the irradiation from the corona and variations in the chromospheric electron density, which will be qualitatively reproduced by our SE approach. We do not attempt a detailed analysis of the line profiles because they will be quantitatively affected by NE effects.

Coronal radiation We include radiation emitted in the corona by adding a coronal emissivity:

$$\psi_\nu = \Lambda_\nu(T) n_e n_H, \tag{2}$$

where ψ_ν is the emissivity in units of power per solid angle per frequency per volume, n_e and n_H are the electron density and hydrogen density and $\Lambda_\nu(T)$ is the emissivity per hydrogen atom per electron. The quantity $\Lambda_\nu(T)$ was computed using the CHIANTI package version 7.1 (Dere et al. 1997; Landi et al. 2013). For a grid of 121 temperatures, logarithmically spaced between 1 kK and 10 MK, we computed the radiative losses assuming coronal equilibrium ionisation balance for all lines in the CHIANTI database using the abundance given in the file `sun_coronal.abund` and the ion fractions given in the file `chianti.ioneq`. We removed all lines from hydrogen and helium because they are accounted for already in *Multi3d*: helium as the active non-LTE atom and hydrogen as a background opacity source. The resulting emissivity was binned into 0.1 nm wide bins such that the frequency integral yields the total radiative losses at that temperature. This table was remapped to the coarser frequency grid used in *Multi3d* while conserving the frequency integral.

The ionisation state in the time-varying corona is not in equilibrium (e.g., Joselyn et al. 1979; Hansteen 1993; Bradshaw & Raymond 2013), and this will have an effect on the coronal emissivities. While it is possible to run *Bifrost* with non-equilibrium coronal ionisation (Olluri et al. 2013b), it is computationally prohibitively expensive to include all elements and atomic levels present in the CHIANTI line list. We therefore opted for the simpler and faster coronal equilibrium approximation.

3. Observations

The observations were taken on 2015-07-31 from 08:46:36 UT to 08:50:18 UT with the TRIPPEL spectrograph (Kiselman et al. 2011) at the Swedish 1-m Solar Telescope (SST, Scharmer et al. 2003) on La Palma. We obtained raster scans of active region NOAA 12393 at a viewing angle $\mu = 0.76$, recorded in reasonable but not excellent seeing conditions. The raster scan contains 300 slit positions with a step size of 0.″1 and a slit width of 0.″11. The field-of-view is $30'' \times 34.''2$. It took 222 s to record the full scan.

The SST was used for the first time to observe in the infrared, employing an OWL-camera (OWL SW1.7 CL-640). The recorded spectral region ranges from 1081.84 nm to 1083.49 nm featuring the He I 1083 nm and Si I 1082.7 nm spectral lines. The estimated spectral resolution of TRIPPEL is $\lambda/\delta\lambda \approx 150,000$ as determined by comparing with a high resolution reference spectrum (Kiselman et al. 2011).

The sensor of the OWL-camera has a size of 640×512 pixels with a spectral dispersion of 2.6 pm/pixel and a spatial scale of 0.″067 pixel^{-1}. The spectra were rebinned in the spatial direction to a scale of 0.1 arcsec/pixel to create square pixels in the raster scan. We took three acquisitions in each slit position with an

exposure time of 100 ms each, with a 0.74 s cadence per slit position. For each slit position we used the acquisition that had maximum continuum contrast.

We reduced the spectra using the TRIPPEL pipeline (Pereira et al. 2009; Kiselman et al. 2011). The reduction steps consist of flat field and dark frame corrections, geometrical corrections for smile and keystone and a wavelength calibration. The spectra were corrected for stray-light and hot pixels were removed from the spectra.

The SST observations were accompanied by observations with the Interface Region Imaging Spectrograph (IRIS, De Pontieu et al. 2014). The IRIS continuum channel at 283.2 nm was used for alignment with the SST raster scan continuum image: First, the IRIS slit-jaw images were interpolated to the scale of the SST raster scan, rotated and aligned with the slit jaw image. Second, to correct for higher-order shifts due to seeing, we applied a destretching routine from the CRISPRED pipeline (de la Cruz Rodríguez et al. 2015) to the SST raster scan with the seeing-free IRIS 283.2 nm continuum image taken half-way during the SST scan as an anchor. As a result of this correction, we are confident that the alignment has accuracy of $\sim 0\farcs2$ which is below the IRIS resolution of $\sim 0\farcs35$.

We also make use of co-spatial and co-temporal data taken with the Atmospheric Imaging Assembly (AIA, Lemen et al. 2012) on board the Solar Dynamics Observatory (SDO, Pesnell et al. 2012). These data were co-aligned with the IRIS and SST data to within an accuracy of one AIA pixel,

In this paper we compare the SST raster scan with IRIS Si IV 140 nm slit-jaw images (from now on Si IV SJI) and the AIA data. Therefore, we created an artificial raster scan with the same slit positions and cadence as the SST raster scan from the Si IV SJI images. Each column in this artificial raster scan equals the column in the Si IV SJI which is the nearest neighbour in time to the SST acquisition time of the column. Due to the big difference in cadence (0.74 s per slit position in the SST and 17 s cadence for the Si IV SJI), only 14 slit-jaw images are used to compose this artificial raster scan. Artificial rasters of the AIA data (12 s cadence) where created in the same way as was done for the IRIS data.

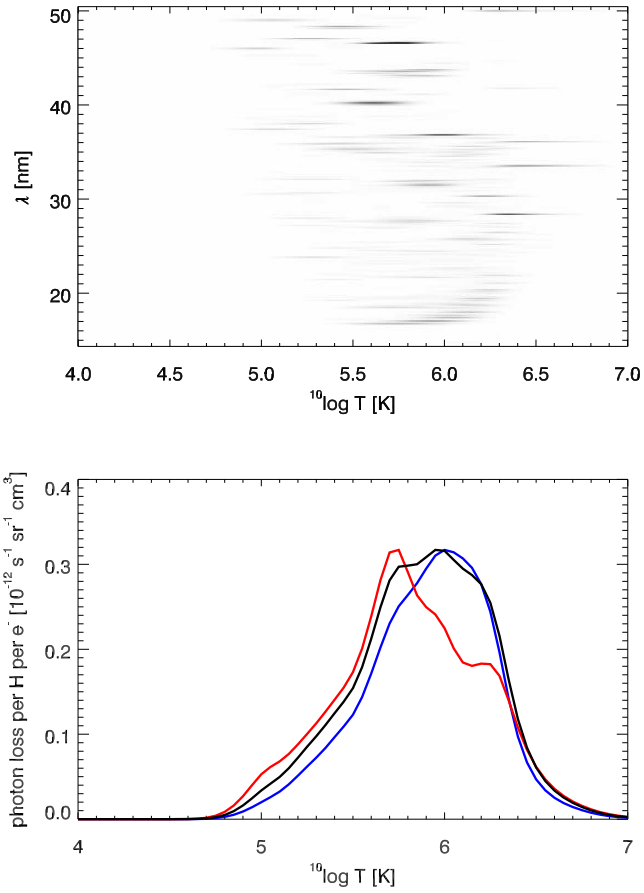

Fig. 2. Top: Coronal radiation losses per hydrogen atom per electron ($\Lambda_\nu(T)$ in Eq. 2) as function of temperature and wavelength. The scale is inverted, so black means large losses. Bottom: Λ_E, the frequency-integrated energy losses per hydrogen atom per electron (blue, arbitrary units); Λ_{ph}, the frequency-integrated photon losses per hydrogen atom per electron (black, scale on the left); Λ_{csw}, the frequency-integrated, He I ground-state continuum cross section weighted, photon losses per hydrogen atom per electron (red, arbitrary units).

4. Results

4.1. Coronal sources of ionising radiation in the He I ground state continuum

Our 3D Bifrost model includes the lower corona with variations in temperature and density, so it should mimic the observed behaviour. We investigate systematically how the EUV radiation is produced.

As a first check we compared the average UV flux in our model to the values in the "low activity model" of Tobiska (1991). Newer models are available (see Tobiska 2004), but the 1991 model is sufficiently accure for our purposes. We integrated the average vertically emerging intensity in our model from 14.3 nm to 50.4 nm, the range over which we include absorption and emission in the He I ground state continuum, and found a value of 48 W m^{-2} ster^{-1}. This is $\sim$ 60% higher than the corresponding value computed from Tobiska (1991). We thus conclude that our model produces a UV flux in the He I ground state continuum comparable to observations.

Note that we do not include absorption in the He I continuum below 14.3 nm, for which Tobiska gives 3.7 W m^{-2} ster^{-1}, so the error is small. Also note that the Tobiska results are consistent with newer observations with AIA/EVE (Woods et al. 2012).

In Fig. 2 we show $\Lambda_\nu(T)$ in Eq. 2 for $\lambda < 51$ nm. The strongest emission feature is a Ne VII resonance line at 46.522 nm at $\log_{10} T = 5.7$. The blue curve in the bottom panel shows $\Lambda_E = \int_{\nu_{\min}}^{\nu_{\max}} \Lambda_\nu \, d\nu$, the losses integrated over the frequency range in which we include He I ground state continuum opacity in our model atom. This distribution peaks at $\log_{10} T = 6$.

In black we show the frequency-integrated photon losses, to take into account that each emitted photon can only ionise one He I atom (we omit the integration bounds for brevity):

$$\Lambda_{\rm ph} = \int \frac{\Lambda_\nu(T)}{h\nu} \, d\nu. \tag{3}$$

The photon-energy weighting increases the relative contribution of lower-temperature gas to the He I photoionisation because of the weighting with the inverse frequency. Finally we computed the coronal photon losses as the He I ground state continuum experiences it, by also weighting with the photoionisiaton cross section:

$$\Lambda_{\rm csw} = \int \sigma_\nu \frac{\Lambda_\nu(T)}{h\nu} \, d\nu, \tag{4}$$

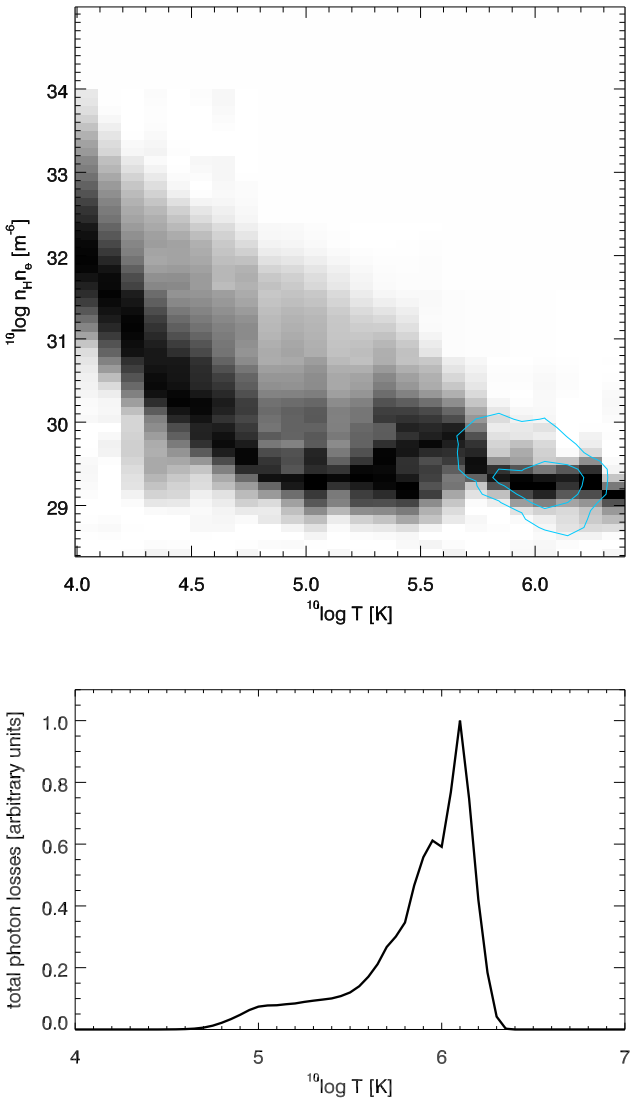

Fig. 3. Top: Scaled joint probability density functions (JPDF) of $n_H n_e$ versus T in the chromosphere and corona of our simulation snapshot. The inner blue contour includes 50% of all pixels, the outer contour 75%. Each column in the panels is scaled to maximum contrast to increase visibility. Bottom: volume-integrated, frequency integrated and cross-section weighthed photon losses as function of temperature in our simulation snapshot (i.e., $\int_V L_{\rm csw}\,{\rm d}V$ in Eq. 5).

shown in red in the bottom panel of Fig. 2. The peak of the distribution then shifts to $^{10}\log T = 5.7$ K, owing to the Ne VII line. In summary, the He I ground state continuum is sensitive to radiation emitted at a wide range of temperatures, with peak sensitivity at 500 kK plasma.

We now proceed to investigate the effect of the density variations in the transition region and corona of the atmosphere model. Figure 3 shows the distribution of $n_H n_e$ versus the temperature in the chromosphere and corona of our simulation snapshot. The majority of the volume is filled with gas at coronal temperatures, but this gas has a relatively low density. The colder material at transition-region temperatures occupies a much smaller volume, but has a much higher density. Combining all ingredients we finally arrive at the bottom panel of Fig. 3, which shows

$$\int_V \Lambda_{\rm csw} n_H n_e \,{\rm d}V = \int_V L_{\rm csw}\,{\rm d}V \tag{5}$$

the cross-section weighted total production of ionising photons in our simulation volume V as function of temperature. The majority of the photons are produced by the tenuous coronal gas but there is a significant tail toward transition region temperatures.

In Fig. 4 we show the effect of the spatial variation of $L_{\rm csw}$. Panels a–c show $L_{\rm csw}$ integrated along the x,y, and z-axis, respectively. The distribution along 2D cross cuts are given in the accompanying animation. The emission (red colors in the animation) is highly structured, and peaks in a thin sheath just above the chromosphere.

The resulting cross-section weighted radiation field $J_{\rm csw}$ impinging on the chromosphere is shown in panel d of Fig. 4. It shows a good correlation with the locations of strong emission on large scales, but not on small scales. This is because the radiation field at location $\boldsymbol{r}$ is in essence the integral of the emissivity weighted with the inverse distance squared:

$$J_{\rm csw}(\boldsymbol{r}) \approx \int_0^\infty \int_V \frac{4\pi}{h\nu}\sigma_\nu \frac{\psi_\nu(\boldsymbol{r}')}{|\boldsymbol{r}-\boldsymbol{r}'|^2} {\rm e}^{-\tau(\boldsymbol{r},\boldsymbol{r}')}\,{\rm d}\boldsymbol{r}'{\rm d}\nu, \tag{6}$$

with $\tau(\boldsymbol{r},\boldsymbol{r}')$ the optical thickness between points $\boldsymbol{r}$ and $\boldsymbol{r}'$, and the integral over $\boldsymbol{r}'$ is taken over all space. The emissivity is mainly due to the corona where the extinction is negligible, and the extinction is essentially chromospheric. Therefore $J_{\rm csw}$ is sensitive to both strong, closely located sources as well as larger regions at larger distances. The column-integrated lower level population of the He I 1083 nm shows a similar large scale correlation (panel e, the actual level population per volume is shown in blue in the animation). In panel f we show the resulting image at the nominal line center wavelength, which shows fine structuring up to a scale of a fraction of a Mm.

Note that the term ${\rm e}^{-\tau(\boldsymbol{r},\boldsymbol{r}')}$ contains significant complexity. It encodes the different opacity at different wavelengths, not only for helium but also for the main other absorber, which is the hydrogen Lyman continuum. Assuming all hydrogen and helium neutral, then the He I ground state continuum makes up 40% of the total chromospheric opacity at 50 nm and 70% at 15 nm. Our analysis thus somewhat overestimates the effect of long-wavelength photons, because $\Lambda_{\rm csw}$ does not take this wavelength dependence into account

Figure 4 and the animation show that the high emissivity points are located close to the chromosphere These will thus contribute most to the high $J_{\rm csw}$ in the nearby chromosphere. In Fig 5 we show the temperature distribution of the high-L points. It peaks at 100 kK, indicating that the emission is coming from the transition region. Inspection of the cross-section-weighted emissivities computed with CHIANTI at $T = 100$ kK and $n_e = 10^{16}$ m^{-3} show that only 37 lines of C III, C IV, N III, Ne II, Ne III, Ne IV, and C III produce 88% of the ionising photons.

In summary, we have shown that in our model the main source of the small-scale variation of ionizing radiation in the He I ground state continuum is a thin shell of relatively dense material at 100 kK in the transition region. Whenever a pocket of chromospheric material is sufficiently illuminated by this material it develops appreciable opacity in the He I 1083 nm. This mainly occurs in material that is almost completely surrounded by TR material, i.e., slender extensions of the chromosphere that protrude into the corona.

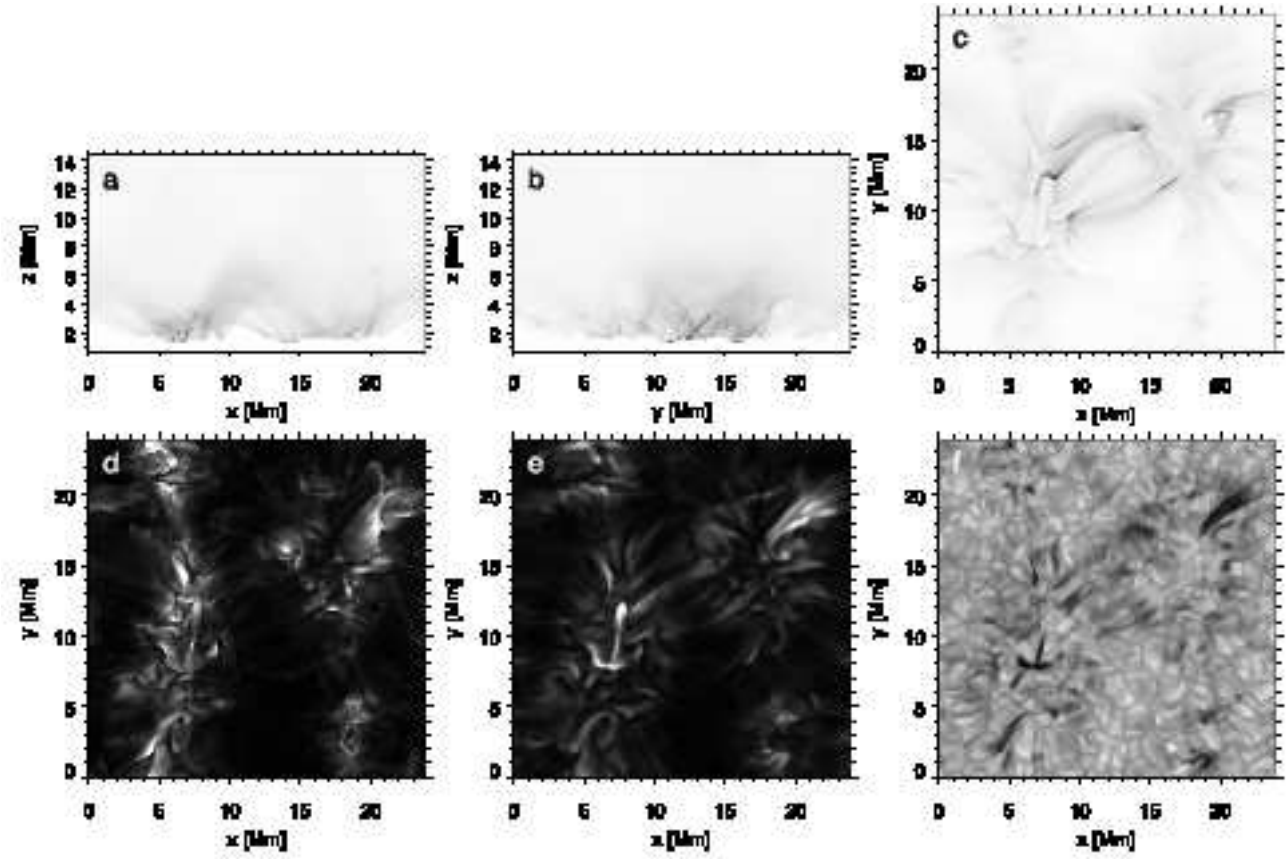

Fig. 4. Spatial relation between coronal emissivity and opacity in He I 1083 nm. Top row: frequency integrated and cross-section weighted photon losses $L_{\rm csw}$, integrated along the *y*-axis (a), the *x*-axis (b) and the *z*-axis (c), on an inverted brightness scale. Panel (d): the resulting angle-averaged radiation field at the largest height in each column where $T = 15$ kK, showing the spatial variation of the ionising radiation impinging on the chromosphere. Panel (e): total depth-integrated column density of the lower level of the He I 1083 nm. Panel (f): vertically emergent intensity at the nominal line core of the He I 1083 nm. This figure has an accompanying movie in the online material. The movie shows 2D cross-cuts through the simulation domain, with $\Lambda_{\rm csw}$ in red and the He I 1083 nm lower level population in blue

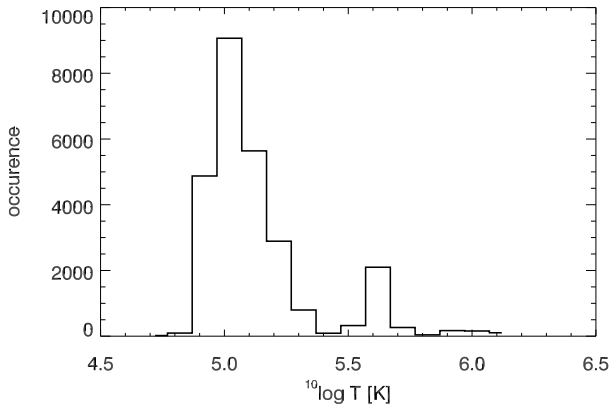

Fig. 5. Histogram of the temperature of the gas for grid points in the model with $L_{\rm csw} > 0.01\,\max(L_{\rm csw})$.

4.2. Other sources of ionizing UV radiation

Besides radiation from bound-bound transitions in the TR and corona, there are other sources of ionising radiation. The most important contributions are the He II ground state continuum, the He II 30.4 nm line and the hydrogen Lyman continuum. The first two are included self-consistently in statistical-equilibrium non-LTE because they are included in the model atom. The latter is included as a background element in the following way: the hydrogen level populations are taken from the *Bifrost* model, where they were computed including non-equilibrium ionisation effects (Golding et al. 2016). The Lyman continuum is treated as a background process in our approximation, which means we assume coherent scattering and a photon destruction coefficient computed using the Van Regemorter approximation. We solved the 3D non-LTE radiative transfer problem both with and without the coronal emissivities to investigate the importance of the hydrogen Lyman and He II continua on the He I 1083 nm opacity.

Figure 6 compares both computations. Ignoring the coronal emissivity leads to much lower total chromospheric column density, and thus optical thickness, for the He I 1083 nm, on average a factor 6.3 less (panel a and b). The resulting optical thickness is too low to leave a strong visible imprint in the intensity images at the line core. Only at a few locations is the photoionisation of He I by He II and H I radiation strong enough to be clearly visible. The best example is the upside-down T-shaped dark feature at $(x, y) = (7, 8)$ Mm.

The frequency-integrated spatially-averaged intensity of the He II 30.4 nm line in our model is 13 W m^{-2} ster^{-1}, which is about 27% of the total intensity between 14.3 and 50.4 nm. This is somewhat higher than the observed values of MacPherson & Jordan (1999), who measured 5 W m^{-2} ster^{-1} for internetwork and 10 W m^{-2} ster^{-1} for a strong network boundary. So while our computation of the He II 30.4 nm line might be deficient in

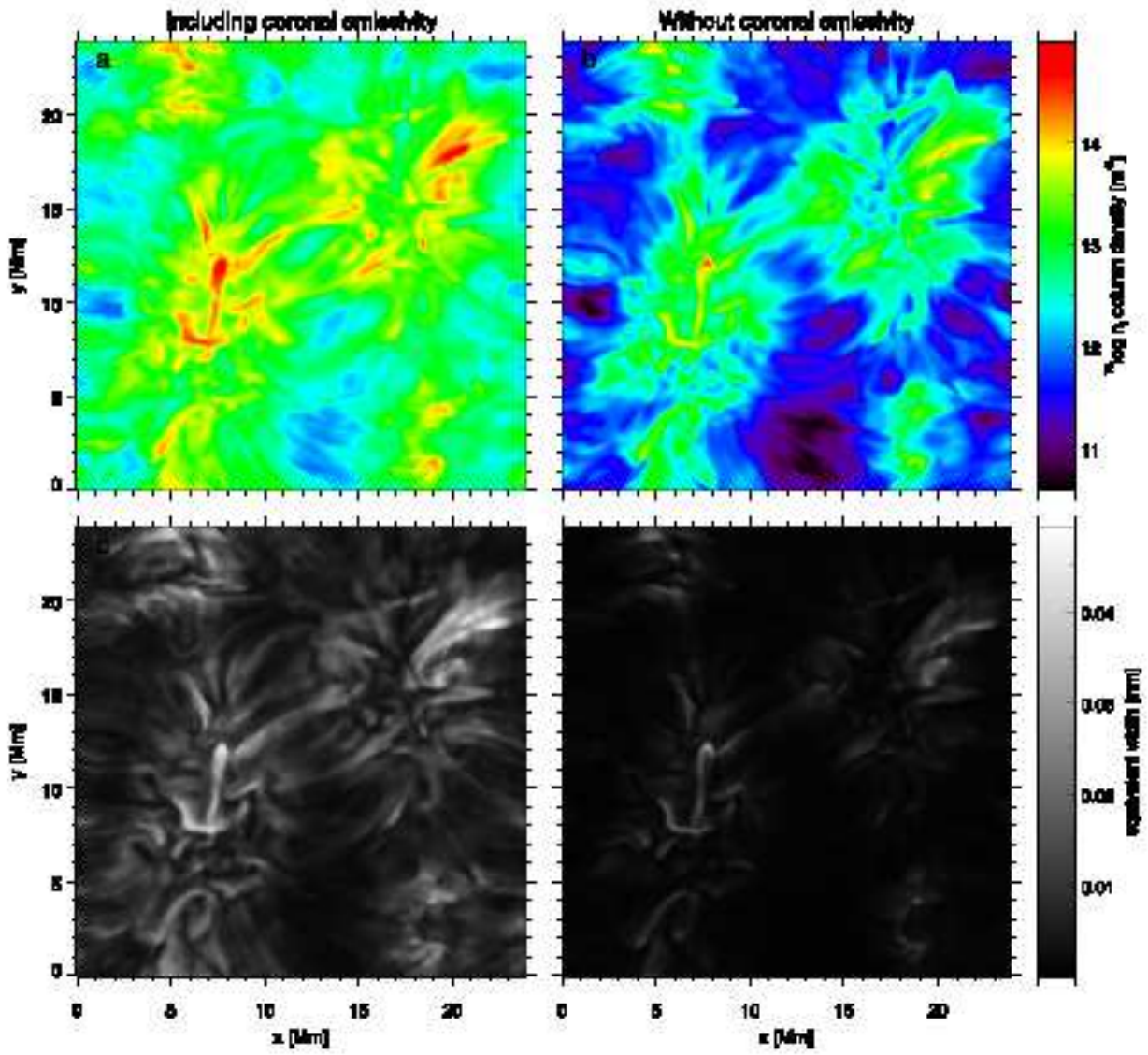

Fig. 6. Demonstration of the importance of radiation from the corona and transition region for the photoionisation in the He I ground state continuum. Panels a and b compare the column integrated lower-level population of the He I 1083 nm line with (a) and without (b) the inclusion of coronal and TR emission. Panels c (with emission) and d (without emission) compare the resulting equivalent widhts of the He I 1083 nm line.

the sense that we ignore non-equilibrium effects, it nevertheless produces roughly the right intensity. We thus conclude that the line is an important, but not dominant, source of ionizing photons in the He I ground state continuum.

4.3. Importance of direct collisional excitation

We computed the $N_{\rm hot}$, total number of He I atoms in the lower level of the He I 1083 nm line in our model chomosphere, transition region and corona, for those grid points with a temperature above 20 kK, and computed $N_{\rm cold}$, the same quantity but now for those points where $T < 20$ kK. We find that $N_{\rm hot}/N_{\rm cold} = 0.005$, and thus conclude that direct collisional excitation is an insignificant source of He I 1083 nm opacity in our statistical equilibrium computation.

4.4. 3D effects on the UV illumination

The coronal UV radiation spreads out in 3D. We test the importance of the horizontal spreading by comparing a computation using the full 3D radiation field (3D) and a computation where each column in the model atmosphere is treated as an independent plane-parallel atmosphere (1D). In Fig. 7 we show the differences between the two computations.

Panels a and b compare the UV radiation field in a vertical slice through the model. Panel b show vertical striping in J, typical for 1D calculations, whereas the 3D computations has a more even distribution. Notice however that the 3D computation also shows artefacts: the diagonal striping is caused by the finite number of ray angles that we use (24 angles). A small volume with high emissivity will thus only illuminate the surrounding space along the ray directions. Because the coronal emissivity is highly structured this shows up strongly. The middle row compares the resulting He I 1083 nm lower level populations along

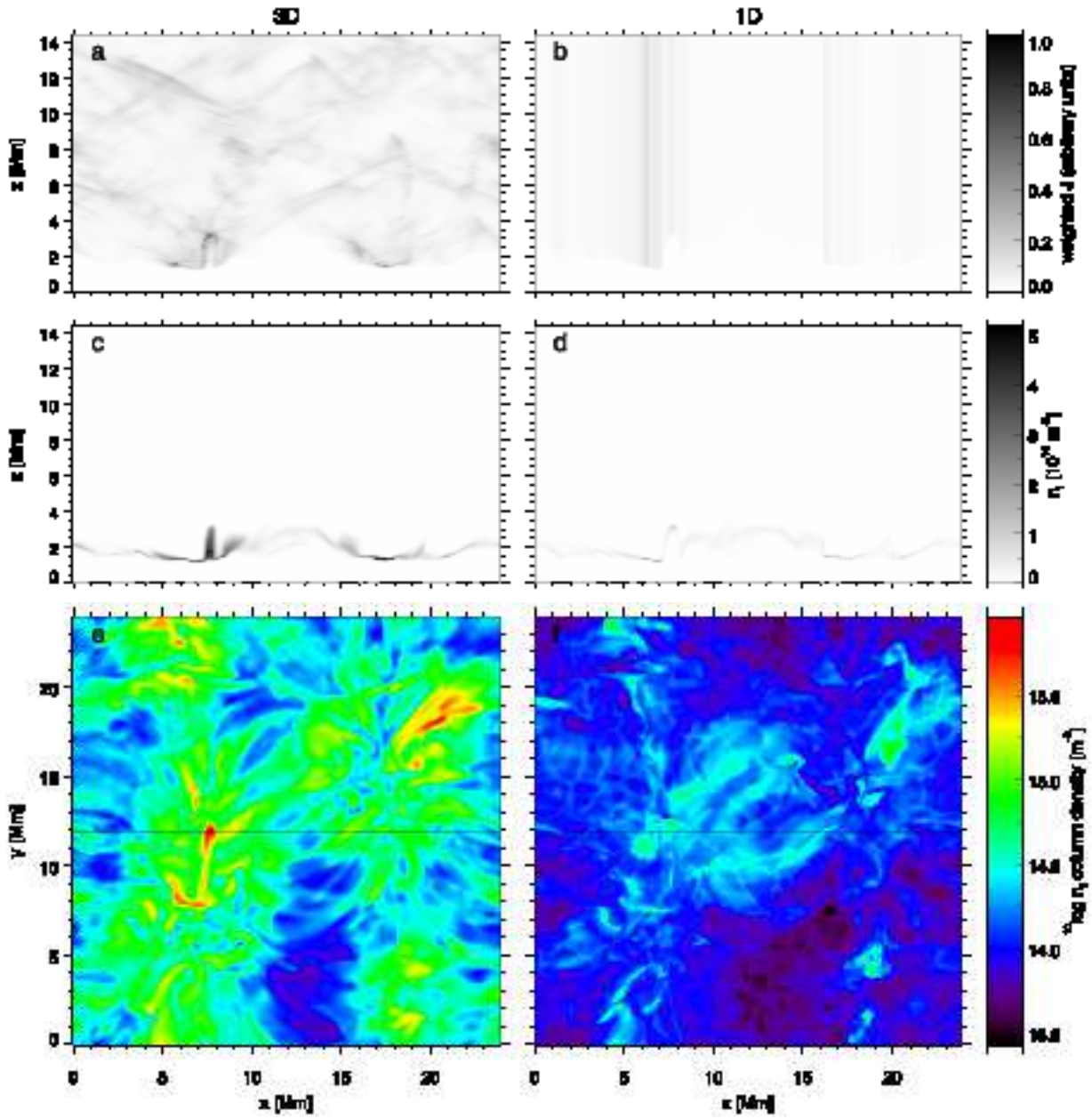

Fig. 7. Comparison of the He I 1083 nm lower-level population assuming 3D radiative transfer (left-hand column) and 1D radiative transfer (right-hand column). Top row: cross-section weighted angle-averaged radiation field in a vertical slice at $y = 11.9$ Mm. Middle row: resulting lower level population of the He I 1083 nm line in a vertical slice at $y = 11.9$ Mm. Bottom row: column integrated lower-level population of the He I 1083 nm line, with the slice used in panels a—d indicated with a black line.

the same vertical slice. In 3D the population is much higher than in 1D. This is mainly due to the effective self-shielding in 1D geometry, because radiation can only come from one direction. In 3D extensions of chromospheric material into the corona can be illuminated from all sides. A clear example can be seen at $(x, z) = (7.5, 2.0)$ Mm, where a finger of chromospheric material is surrounded by high-emissivity TR/coronal material. Similar effects were already reported by Carlsson & Leenaarts (2012), who investigated 3D effects on the heating of the chromosphere by UV radiation produced in the corona.

Finally, in panels e and f we compare the spatial distribution of the total column density of the lower-level population of the He I 1083 nm line. In 3D it is on average 4.2 times higher than in 1D, and its maximum is 6.8 times higher.

4.5. 3D effects on the source function

At the height in the chromosphere where the He I 1083 nm line has appreciable opacity, the mass density is so low that the damping wings of the Voigt profile are negligible, and the extinction coefficient is essentially Gaussian. The photon destruction probability ϵ in the He I 1083 nm is of the order 10^{-4} – 10^{-2}. The line is thus scattering dominated ($S_\nu \simeq \bar{J}_{\nu 0}$) and the thermalisation depth is located at a line core optical depth $\tau \cong 1/\epsilon = 10^2$ – 10^4. This is at least eleven times the maximum optical thickness of the line-forming region in our model, which is 8.9. So the source function thermalises in the photosphere, even when the line-forming region in the chromosphere is optically thick. We thus expect strong 3D effects on the source function.

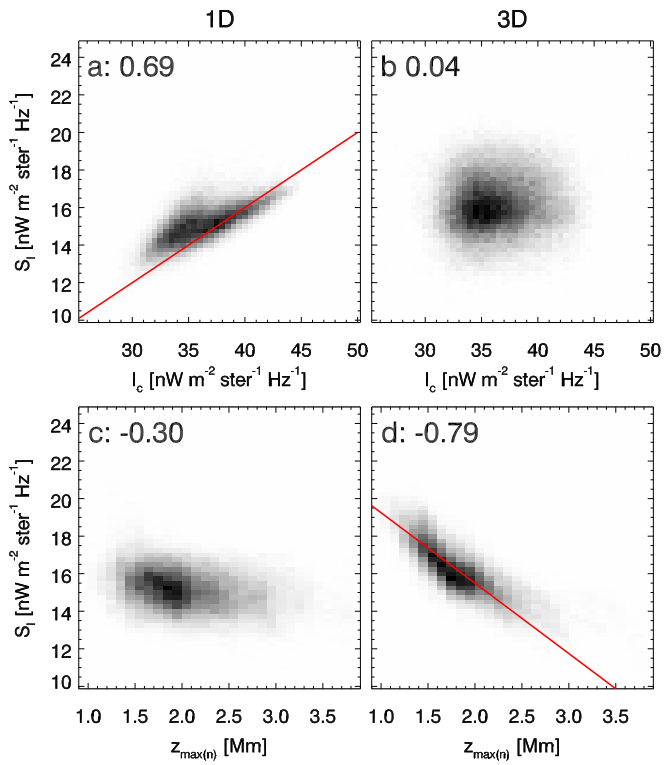

Fig. 8. JPDFs of the He I 1083 nm source function and the continuum intensity and the height where the line opacity is largest. The red line in panel a is $S_1 = 0.4I_c$. The red line in panel d is $S_1 = 23 - 3.75z_{\max(n)}$

We investigated this effect by comparing the full 3D computation with the 1D column-by-column computation. The top row of Figure 8 shows joint probability density functions (JPDFs) of the line source function S_1 and the underlying continuum intensity I_c computed from each (x, y)-pixel in our model, for both the 3D and 1D computation.

Panel a shows a strong correlation between S_1 and I_c in the 1D computation. The red line shows that roughly speaking, $S_1 = 0.4I_c$. This is consistent with Avrett et al. (1994) who obtained the same relation for 1D semi-empirical models illuminated with a prescribed UV radiation field. In 3D this correlation is gone (panel b). The reason is that the source function at a given location in the chromosphere is no longer correlated to the continuum intensity from the photosphere directly below it, but by a spatial average of the continuum intensity emitted from an extended region encompassing multiple granules.

The bottom row of Figure 8 shows the JPDFs for S_1 and the height where the lower-level population is maximum in the chromosphere $z_{\max(n)}$. In 1D there is just a rather weak correlation between the two quantities, which only shows up in the correlation coefficient. In 3D it is strong, and is clearly visible in the JPDF as well.

The behaviour of the He I 1083 nm source function is similar to the source function in the Hα line (Leenaarts et al. 2012). Both lines have source functions that thermalise in the photosphere, both lines are strongly scattering and both lines have negligible opacity in the upper photosphere and lower chromosphere.

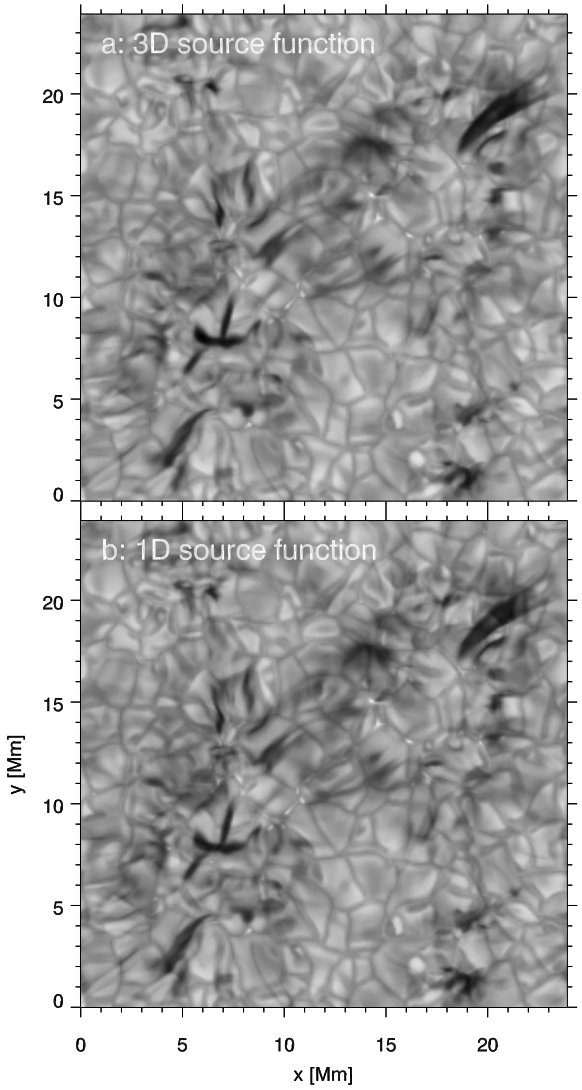

Fig. 9. Comparison of the synthetic He I 1083 nm line intensity computed with the correct 3D source function (upper panel) and an approximate 1D source function in the chromosphere (lower panel).

4.6. Relative importance of 3D in the UV illumination and source function

In order to assess the relative importance of 3D effects in the UV illumination and the source function we did a test calculation where we computed the emergent intensity using the opacity from the 3D computation, but used a line source function of the form

$$S_1(x, y, z) = 0.4I_c(x, y), \tag{7}$$

which was shown in Section 4.5 to be a decent approximation of the source function as obtained from 1D plane-parallel computations. The resulting line-center intensity image, together with the 3D computation, is shown in Fig 9. Both images are very similar in absorption structure, so we conclude that 3D effects in the UV illumination are the most important for the He I 1083 nm formation, while 3D effects on the line source function are minor.

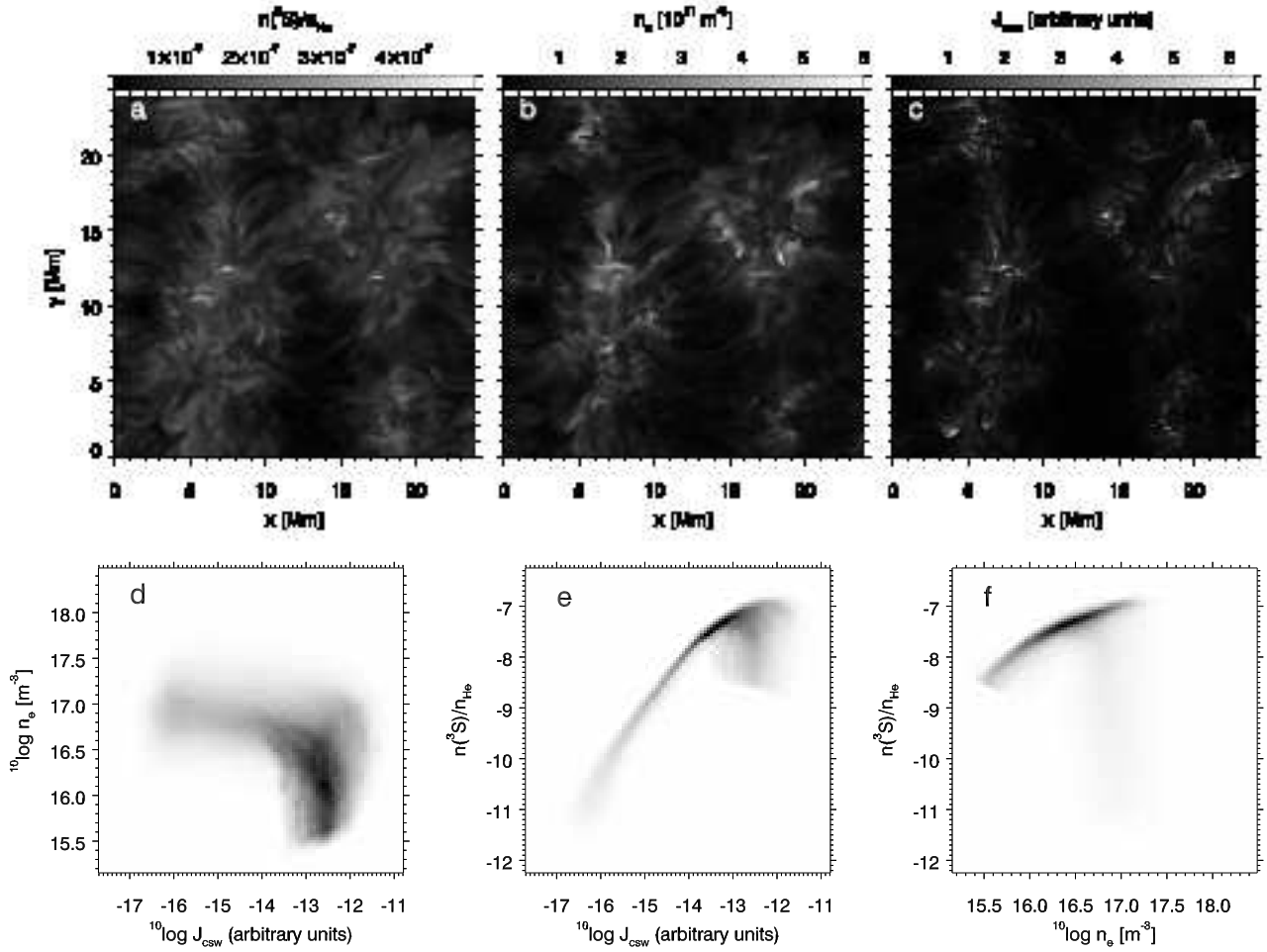

Fig. 10. Relation between He I 1083 nm opacity, electron density and the coronal irradiation. Panel a: relative population of the He I 1083 nm lower level, for each pixel at the height in the chromosphere where the relative population has a maximum. Panel b: electron density at the same location as in a. Panel c: J_{csw} at the same location as in a and b. Panel d: JPDF of J_{csw} and the electron density in the chromosphere. Panel d: JPDF of J_{csw} and the relative population of the He I 1083 nm. Panel f: JPDF of the electron density and the relative population of the He I 1083 nm.

4.7. *Variation in* He I *1083 nm opacity and the chromospheric electron density*

In the previous subsections we explored the origin and effect of the ionising radiation. In this subsection we discuss the combined influence of the electron density and the radiation. Equation 1, which was derived by Livshits et al. (1976), predicts a correlation between the relative population $n(2s\,^3S)/n_{He}$ of the He I 1083 nm, and those quantities. We illustrate this in Fig. 10. For each (x, y) location in the model we looked up the location in the chromosphere where $n(2s\,^3S)/n_{He}$ has a maximum. For those locations we extracted $n(2s\,^3S)/n_{He}$, n_e, and J_{csw} and display the resulting maps in panels a–c. The map of $n(2s\,^3S)/n_{He}$ is finely structured on small scales, but appears relatively smooth on larger scales. The electron density map shows a substantial correspondence with the $n(2s\,^3S)/n_{He}$ map. The map of J_{csw} in panel c is, in contrast, much more intermittent.

In panels d–f we put the correlation on a more precise footing. Panel d shows the joint probability density function of J_{csw} and n_e. It shows a peculiar ¬-shape. Panel e shows the JPDF of J_{csw} and $n(2s\,^3S)/n_{He}$. It consists of two distinct components, a tight positive correlation that roughly follows the prediction of Eq. 1 for fixed electron density and a beard-shaped cluster of points of $-13 < \log_{10} J_{csw} < -12$. In panel d it can be seen that the latter points correspond to a sudden large spread in values of the electron density, and thus a much weaker correlation between J_{csw} and $n(2s\,^3S)/n_{He}$. A similar effect appears in the JPDF of n_e and $n(2s\,^3S)/n_{He}$: there is a component with a tight correlation and for $16.5 < \log_{10} n_e < 17$ there is a beard-like extension downward, caused by the large spread of values in J_{csw} at those electron densities, as shown in Panel d.

We thus conclude that the approximate formula made by Livshits et al. (1976) is validated by our 3D non-LTE radiative transfer computations.

5. Correlation with Si IV 1393 and 1402 and AIA 304, 171,193 and 335 emission

In Sec. 4.1 we showed that the source of the most intense He I ground state continuum radiation impinging on the chromosphere in our simulation comes from gas with a temperature of about 100 kK. This temperature is close to the coronal-equilibrium peak formation temperature of the Si IV lines at 139.38 nm and 140.28 nm, which is at $\log T = 4.8$ K. These lines dominate the emission in the 140 nm slit-jaw imager of IRIS.

In Fig. 11 we compare a synthetic Si IV SJI image computed from our simulation snapshot and a map of the column-integrated L_{csw}, i.e, $\int L_{csw}\,dz$. The brightest Si IV SJI emission

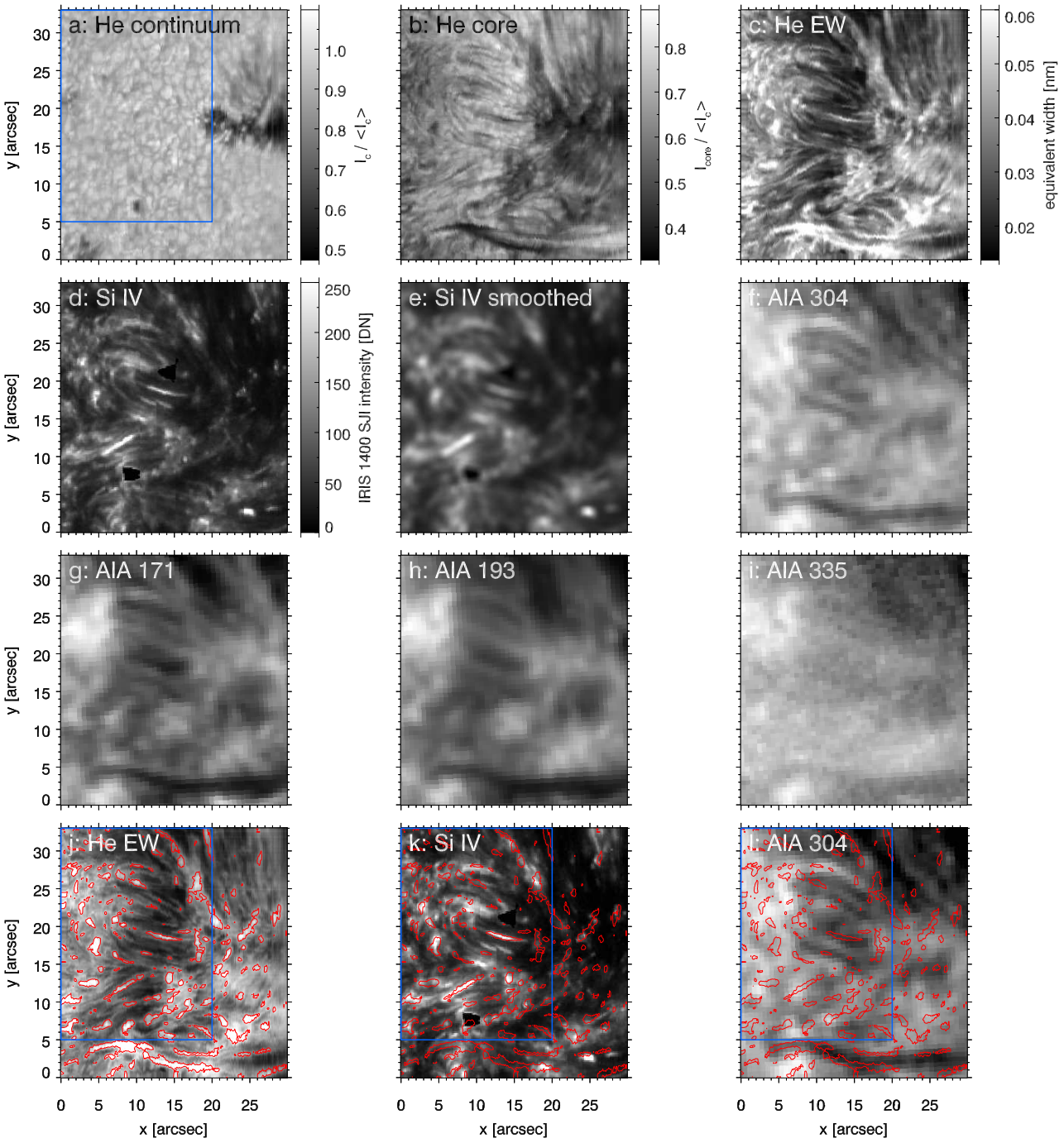

Fig. 12. Co-spatial and co-temporal observations of active region NOAA 12393 with the SST, IRIS and SDO/AIA. a) TRIPPEL raster scan image in the continuum at 1081.971 nm. b) TRIPPEL raster scan image of the profile minimum of He I 1083 nm. c) TRIPPEL raster scan image of the equivalent width of He I 1083 nm. d) artificial raster scan constructed from the IRIS 140 nm SJI images which are dominated by Si IV emission. e) same as d, but now smoothed to AIA resolution. f)–i) artificial raster scans for the AIA band given in the panels. j)–k): same as c, d, and f, but now with contours of local maxima in the EW overplotted in red. The blue box outlines the area discussed in the text.

corresponds to the brightest $L_{\rm csw}$, but the latter is more extended and has a diffuse component, owing to the large variety of lines that contribute to it.

The bottom panel of Fig 11 shows a histogram of $L_{\rm csw}$ for all grid points in the simulation in black. In red it shows a histogram of $L_{\rm csw}$ for only those grid points that belong to the 0.1% grid points that have the highest Si IV SJI emmisivity. This confirms quantitatively that locations with very high Si IV emission indeed correspond to locations with the highest $L_{\rm csw}$.

Based on the results shown in Fig. 11 and the rough correlation between $L_{\rm csw}$ and the lower-level population of He I 1083 nm (see Fig. 4), we thus expect a considerable correlation between Si IV emission and He I 1083 nm strength on scales of $\sim$ 1 arcsecond. We also show that the bulk of the ionizing photons are coming from hotter gas, emitted in a large volume in the overlying corona. We thus also expect a correlation between He I 1083 nm strength and coronal emission at larger scales. The latter correlation has of course been known for a long time (e.g., Kahler et al. 1983).

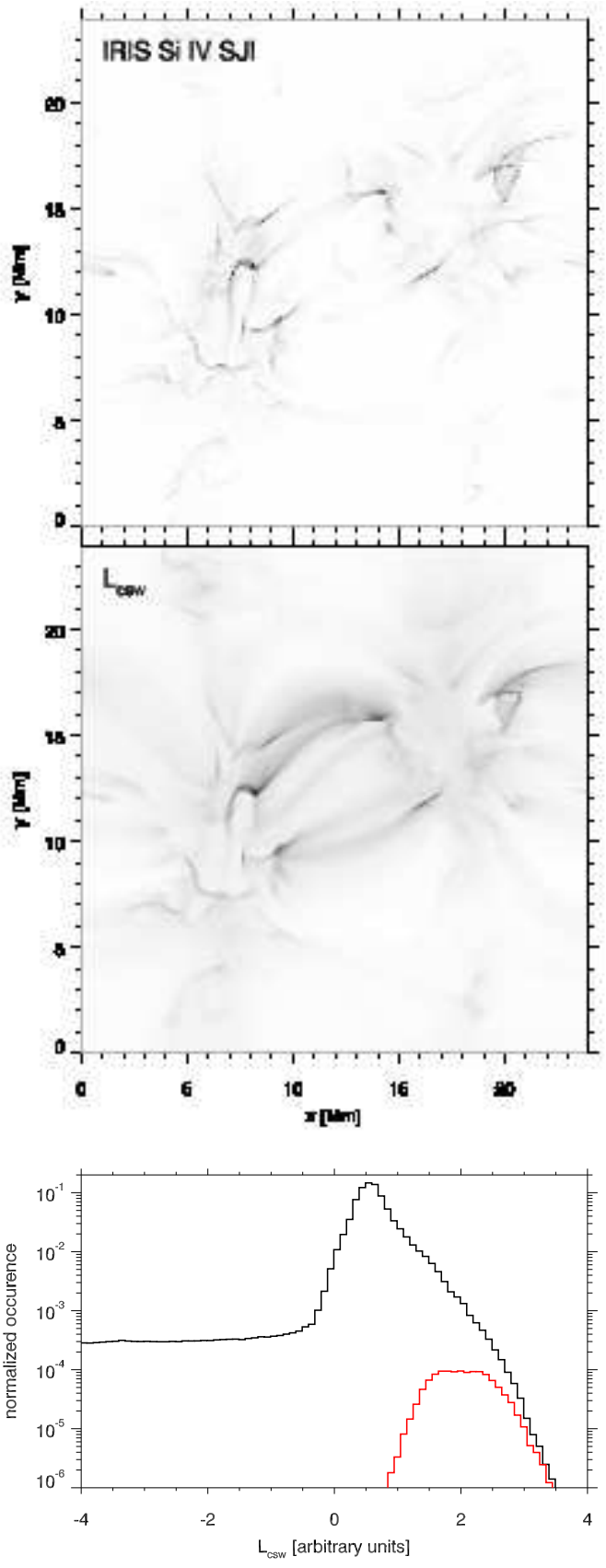

Fig. 11. Comparison of the synthetic IRIS 140 nm slit jaw emission (upper panel) and an image computed from $L_{\rm csw}$, the frequency integrated and cross-section weighted photon losses (middle panel). The bottom panel shows the histogram of $L_{\rm csw}$ for all grid points in the simulation (black) and only for the 0.1% of the grid points that have the highest Si IV emissivity (red).

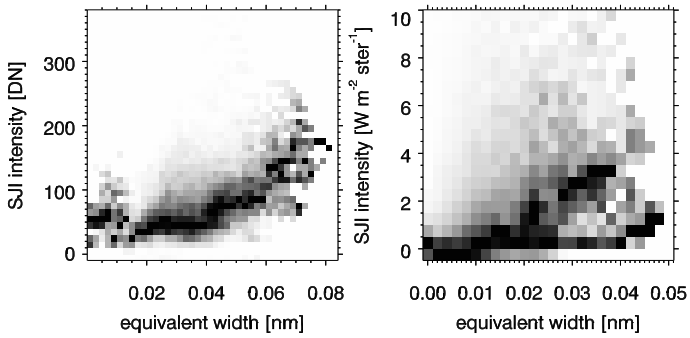

Fig. 13. Joint probability density functions of the equivalent width of He I 1083 nm and Si IV140 nm emission. Left-hand panel: observations; right-hand panel: simulations.

We therefore compared a single raster scan of the He I 1083 nm line taken with the TRIPPEL spectrograph at the SST with co-temporal and co-spatial artificial raster scans constructed from Si IV slit-jaw images and SDO/AIA images (see Sec. 3). Observationally we cannot directly determine atomic level populations, so we took the equivalent width (EW) as a measure instead.

Panel a in Fig. 12 shows the raster scan in a continuum wavelength close to the He I 1083 nm line. There is a small sunspot with an irregular penumbra on the right side of the field-of-view, with granulation and some small pores filling the rest of the panel. Inspection of the IRIS 283.2 Mg II k wing slit-jaw image (not shown) indicates that the observed area shows a considerable amount of magnetic bright points. Panel b shows an image of the He I 1083 nm core. In each pixel the intensity of the profile minimum is taken to compensate for Doppler shifts. The superpenumbra is clearly seen on the right side. The middle part of the image ($5 < x < 20''$) is filled with fibrils with granulation visible in between. The left side of the image shows a more irregular absorption structure. The strong elongated absorption feature at the bottom of the image ($y < 5''$) is an active region filament. Panel c shows the EW of the He I 1083 nm line. The filament has the highest EW, while the areas showing granulation in Panel b have the lowest. Panel d shows the Si IV artificial raster scan. The sunspot is very dark, the filament is not visible, the rest of the image shows filamentary structures with medium brightness and more irregularly shaped patches of high brightness.

The simulation results presented in this paper are not representative for sunspots or filaments. The correlation that we expect on the basis of our simulation and radiative transfer modeling is most likely valid for quiet sun and network areas. We therefore focus on the most quiet area in the observation, roughly speaking where $x < 20''$ and $y > 5''$ (indicated by the blue box in Fig. 12).

Comparison of the brightest areas in panel d with the profile-minimum intensity and EW of He I 1083 nm in panel 12b and 12c shows many places where Si IV brightness coincides with a large He I 1083 nm EW, for example at $(x, y) = (14'', 19'')$, $(x, y) = (7'', 12'')$and $(x, y) = (3'', 23'')$. Careful inspection shows many more locations of good correlation. There are also locations where the correlation is not present, for example at $(x, y) = (10'', 23'')$ and $(x, y) = (11'', 28'')$.

Panels e shows the Si IV emission, smoothed to the same resolution as the AIA data to facilitate a more fair comparison to the emission in the various AIA channels shown in panels f–i, from the coolest 304 channel to the hot 335 channel.

Comparing the AIA 304 channel (panel d, which is most sensitive the He II 30.4 nm emission) to Si IV in panel c, we see that some structures can be recognized in both images, and there is a correlation on large scales. The Si IV image shows considerable more contrast and shows many more small patches of large brightness. The difference in appearance is not only caused by differences in spatial resolution between the IRS and SDO data. The large-scale patches of high EW in panel c correlate roughly with the high-brightness patches in 171 and 193, and to a lesser extent to the 304 and 335 images.

The bottom row (panels j–l) show the EW, Si IV, and 304 image again, but now overlaid with contours enclosing areas of local maxima in EW. These contours where created by thresholding a high-pass-filtered EW image, designed to pick up local maxima in EW, and serve to guide the eye. Inspection of panels k and l shows that the contours of local maxima in EW match the Si IV image much better than the 304 image.

Figure 13 compares the joint probability density function of the He I 1083 nm equivalent width and the Si IV brightness. For the observations we computed it from the area where $x < 20''$ and $y < 5''$ in Fig. 12. For the simulation we degraded the synthetic Si IV image to the spatial resolution of the observations. The observed correlation clearly shows the correlation between high equivalent width and Si IV brightness. For the simulations this correlation is not as strong. The correlation appears as the upper arm of the bifurcated distribution for equivalent widths larger than 0.22 nm.

6. Discussion and Conclusions

In this paper we investigated why the absorption features in images taken in the He I 1083 nm line in quiet Sun and network regions show intricate fine structuring to sub-arcsecond scale using a 3D radiation-MHD simulation of the solar atmosphere, combined with 3D non-LTE statistical equilibrium radiative transfer modeling.

We confirm the mechanism for populating the lower level of the line through photoionisation from the singlet ground state of He I to He II, followed by photorecombination into the He I triplet system as was originally put forward by Goldberg (1939). Direct collisional excitation at temperatures above 20 kK is a negligible source of lower level population in our model. We also confirm the conclusion by Livshits et al. (1976) that the relative opacity of He I 1083 nm is electron density dependent: for a given mass density and coronal illumination the extinction coefficient is an increasing function of the electron density under typical chromospheric conditions.

Our simulations are not representative for strongly magnetically active areas and phenomena, such as emerging flux regions, flares and plage. These are typically associated with elevated chromospheric densities and temperatures and the presence of non-thermal electrons, where population of the triplet system can also occur through direct collisional excitation or collisional ionisation/recombination pathways (e.g., Ding et al. 2005). Our conclusions are therefore not necessarily valid under such circumstances.

We found that the sources of the ionising radiation can be roughly split in two components. The majority of the ionising photons are produced by gas in the 0.5-2 MK temperature range. The source regions are extended as these are the temperatures of typical coronal gas, and their emissivity is relatively low. The second component consists of transition region gas between 80 kK and 200 kK. It produces far fewer ionising photons than the high-temperature component. However, regions of high emissivity of the second component are concentrated in space and are located close to the upper chromosphere. This second, highly structured component is the main cause of variation in the UV flux impinging on the chromosphere. The actual radiation field $J_{\rm csw}$ inside the chromosphere also depends on the shape of the transition region. Chromospheric material that is surrounded by a dense transition region has the highest $J_{\rm csw}$ and consequently the highest He I ground state continuum photoionisation rate.

The He I 1083 nm line strength depends on the integral of the opacity along the line of sight. Therefore dense, vertically-oriented chromospheric structures that are surrounded by hot, dense, transition region and coronal material will typically produce the strongest line.

We tested our predicted correlation between the presence of high-mass-density $\approx$ 100 kK gas and He I 1083 nm absorption by comparing emission in the Si IV 139.38 nm and 140.28 nm lines that form around 80 kK with He I 1083 nm absorption and found that small-scale patches of high He I 1083 nm EW indeed often correlate with high Si IV emission. The correlation is notably absent around the active region filament in our observations, which might indicate a thin and/or low-mass-density transition region around the filament. The correlation between small-scale structure in the EW and AIA 304 is significantly worse. The large-scale variation in EW correlates well with the emission in coronal lines as sampled by the AIA 171 and 193 as well as the AIA 304 emission.

Our work is an improvement over earlier modelling efforts (e.g., Zirin 1975; Pozhalova 1988; Avrett et al. 1994; Centeno et al. 2008). We used a 3D radiation-MHD simulation of the solar atmosphere, as opposed to the 1D models used before. We self-consistently include the emission of ionising radiation from the corona: it is produced by the corona present in the radiation-MHD simulation. Earlier work used a prescribed coronal radiation field.

Despite these improvements there are still a number of limitations to our approach: The simulation that we use produces too little chromospheric dynamics and produces to little chromospheric emission compared to observations (see for example Carlsson et al. 2016; Leenaarts et al. 2013). Increasing the numerical resolution and adding heating effects from ion-neutral interactions (Martínez-Sykora et al. 2012; Khomenko & Collados 2012) might alleviate some of the discrepancy in future simulations. We also base our current analysis on a single snapshot, with a single magnetic field configuration. A future improvement would be to repeat the analysis for a time series of snapshots and for simulation runs with different magnetic field geometries.

The biggest discrepancy in our current analysis is that we do not include the effect of non-equilibrium ionisation in our 3D non-LTE radiative transfer calculation for helium, nor do we include non-equilibrium ionisation effects on the production of ionising photons.

Non-equilibrium ionisation in the transition region and corona typically has the effect that ions in a particular ionisation stage are present over a larger temperature range than what one would expect from coronal equilibrium calculations (Olluri et al. 2013b). The effect on the resulting emissivities and intensities are rather mild for the lines of Si IV, C IV, and O IV that were investigated by Olluri et al. (2015). No non-equilibrium intensity calculations for the lines dominating the He I photoionisation mentioned in at the end of Sec. 4.1 have been done, but the results for the non-equilibrium ionisation balance of oxygen from Olluri et al. (2013a) indicate that O III lines should experience similar mild effects as the O IV lines. Non-equilibrium ef-

fects also play a role for the He II 30.4 nm line (e.g. Golding et al. 2014). However, we showed that the line produces roughly the right amount of photons, so that neglecting this effect has little effect on the formation of the He I 1083 nm line.

Comparisons of one-dimensional calculations assuming SE and NE for helium using the *RADYN* code (e.g., Carlsson & Stein 1992) indicate that large differences in the He I 1083 nm profiles can occur (Golding et al. 2014). While we expect that inclusion of non-equilibrium effects will have large quantitative effects on He I 1083 nm formation, we do not think it will have a qualitative effect on the spatial structure: also in the non-equilibrium case the photoionisation-recombination mechanism is the dominant mechanism populating the triplet states (Golding et al. 2014), The correlation between He I 1083 nm absorption and strong emission in the transition region and high chromospheric electron density will thus remain valid, even though the contribution of direct collisional excitation due to the presence of neutral helium at higher temperatures might play a bigger role. Because we expect quantitative differences when non-equilibrium radiative transfer for helium is taken into account we have refrained from detailed analysis of the synthetic He I 1083 nm profiles in this work.

Acknowledgements. This research was supported by the Research Council of Norway through the grant "Solar Atmospheric Modelling" and through grants of computing time from the Programme for Supercomputing. The research leading to these results has received funding from the European Research Council under the European Union's Seventh Framework Programme (FP7/2007-2013) / ERC grant agreement no 291058. Some computations were performed on resources provided by the Swedish National Infrastructure for Computing (SNIC) at the National Supercomputer Centre at Linköping University. The Swedish 1-m Solar Telescope is operated on the island of La Palma by the Institute for Solar Physics of the Royal Swedish Academy of Sciences in the Spanish Observatorio del Roque de los Muchachos of the Instituto de Astrofísica de Canarias. IRIS is a NASA small explorer mission developed and operated by LMSAL with mission operations executed at NASA Ames Research center and major contributions to downlink communications funded by ESA and the Norwegian Space Centre.

References

Andretta, V. & Jones, H. P. 1997, ApJ, 489, 375
Auer, L. 2003, in ASP Conf. Ser. 288: Stellar Atmosphere Modeling, 3
Avrett, E. H., Fontenla, J. M., & Loeser, R. 1994, Formation of the solar 10830 A line (Infrared Solar Physics, IAU Symp. No. 154, eds. D.M. Rabin, J.T. Jefferies, and C. Lindsey, Kluwer, Dordrecht, pp. 35-47), 35–47
Bradshaw, S. J. & Raymond, J. 2013, Space Sci. Rev., 178, 271
Carlson, B. G. 1963, Methods of Computational Physics, 1
Carlsson, M., Hansteen, V. H., Gudiksen, B. V., Leenaarts, J., & De Pontieu, B. 2016, A&A, 585, A4
Carlsson, M. & Leenaarts, J. 2012, A&A, 539, A39
Carlsson, M. & Stein, R. F. 1992, ApJ, 397, L59
Carlsson, M. & Stein, R. F. 2002, ApJ, 572, 626
Centeno, R., Trujillo Bueno, J., Uitenbroek, H., & Collados, M. 2008, ApJ, 677, 742
Cirtain, J. W., Golub, L., Winebarger, A. R., et al. 2013, Nature, 493, 501
de la Cruz Rodríguez, J., Löfdahl, M. G., Sütterlin, P., Hillberg, T., & Rouppe van der Voort, L. 2015, A&A, 573, A40
De Pontieu, B., Title, A. M., Lemen, J. R., et al. 2014, Sol. Phys., 289, 2733
Dere, K. P., Landi, E., Mason, H. E., Monsignori Fossi, B. C., & Young, P. R. 1997, A&AS, 125, 149
Ding, M. D., Li, H., & Fang, C. 2005, A&A, 432, 699
Fontenla, J. M., Avrett, E., Thuillier, G., & Harder, J. 2006, ApJ, 639, 441
Goldberg, L. 1939, ApJ, 89, 673
Golding, T. P., Carlsson, M., & Leenaarts, J. 2014, ApJ, 784, 30
Golding, T. P., Leenaarts, J., & Carlsson, M. 2016, ApJ, 817, 125
Gudiksen, B. V., Carlsson, M., Hansteen, V. H., et al. 2011, A&A, 531, A154
Gustafsson, B. 1973, Uppsala Astr. Obs. Ann., 5, No. 6
Hansteen, V. 1993, ApJ, 402, 741
Ibgui, L., Hubený, I., Lanz, T., & Stehlé, C. 2013, A&A, 549, A126
Ji, H., Cao, W., & Goode, P. R. 2012, ApJ, 750, L25
Jordan, C. 1975, MNRAS, 170, 429
Joselyn, J. A., Munro, R. H., & Holzer, T. E. 1979, ApJS, 40, 793
Kahler, S. W., Davis, J. M., & Harvey, J. W. 1983, Sol. Phys., 87, 47
Khomenko, E. & Collados, M. 2012, ApJ, 747, 87
Kiselman, D., Pereira, T. M. D., Gustafsson, B., et al. 2011, A&A, 535, A14
Landi, E., Young, P. R., Dere, K. P., Del Zanna, G., & Mason, H. E. 2013, ApJ, 763, 86
Leenaarts, J. & Carlsson, M. 2009, in Astronomical Society of the Pacific Conference Series, Vol. 415, The Second Hinode Science Meeting: Beyond Discovery-Toward Understanding, ed. B. Lites, M. Cheung, T. Magara, J. Mariska, & K. Reeves, 87
Leenaarts, J., Carlsson, M., Hansteen, V., & Rutten, R. J. 2007, A&A, 473, 625
Leenaarts, J., Carlsson, M., & Rouppe van der Voort, L. 2012, ApJ, 749, 136
Leenaarts, J., Pereira, T. M. D., Carlsson, M., Uitenbroek, H., & De Pontieu, B. 2013, ApJ, 772, 90
Lemen, J. R., Title, A. M., Akin, D. J., et al. 2012, Sol. Phys., 275, 17
Livshits, M. A., Akimov, L. A., Belkina, I. L., & Diatel, N. P. 1976, Sol. Phys., 49, 315
MacPherson, K. P. & Jordan, C. 1999, MNRAS, 308, 510
Martínez-Sykora, J., De Pontieu, B., & Hansteen, V. 2012, ApJ, 753, 161
Milkey, R. W., Heasley, J. N., & Beebe, H. A. 1973, ApJ, 186, 1043
Olluri, K., Gudiksen, B. V., & Hansteen, V. H. 2013a, ApJ, 767, 43
Olluri, K., Gudiksen, B. V., & Hansteen, V. H. 2013b, AJ, 145, 72
Olluri, K., Gudiksen, B. V., Hansteen, V. H., & De Pontieu, B. 2015, ApJ, 802, 5
Pereira, T. M. D., Kiselman, D., & Asplund, M. 2009, A&A, 507, 417
Pesnell, W. D., Thompson, B. J., & Chamberlin, P. C. 2012, Sol. Phys., 275, 3
Pietarila, A. & Judge, P. G. 2004, ApJ, 606, 1239
Pozhalova, Z. A. 1988, Soviet Ast., 32, 542
Rybicki, G. B. & Hummer, D. G. 1991, A&A, 245, 171
Rybicki, G. B. & Hummer, D. G. 1992, A&A, 262, 209
Sanz-Forcada, J. & Dupree, A. K. 2008, A&A, 488, 715
Schad, T. A., Penn, M. J., & Lin, H. 2013, ApJ, 768, 111
Schad, T. A., Penn, M. J., Lin, H., & Tritschler, A. 2015, Sol. Phys., 290, 1607
Scharmer, G. B., Bjelksjo, K., Korhonen, T. K., Lindberg, B., & Petterson, B. 2003, in Society of Photo-Optical Instrumentation Engineers (SPIE) Conference Series, Vol. 4853, Innovative Telescopes and Instrumentation for Solar Astrophysics, ed. S. L. Keil & S. V. Avakyan, 341–350
Smith, G. R. 2003, MNRAS, 341, 143
Smith, G. R. & Jordan, C. 2002, MNRAS, 337, 666
Tobiska, W. K. 1991, Journal of Atmospheric and Terrestrial Physics, 53, 1005
Tobiska, W. K. 2004, Advances in Space Research, 34, 1736
Woods, T. N., Eparvier, F. G., Hock, R., et al. 2012, Sol. Phys., 275, 115
Zarro, D. M. & Zirin, H. 1986, ApJ, 304, 365
Zirin, H. 1975, ApJ, 199, L63